



Article

Monitoring Thermal Pollution in Rivers Downstream of Dams with Landsat ETM+ Thermal Infrared Images

Feng Ling ^{1,*} , Giles M. Foody ² , Hao Du ³, Xuan Ban ¹, Xiaodong Li ¹, Yihang Zhang ¹ and Yun Du ¹

¹ Institute of Geodesy and Geophysics, Chinese Academy of Sciences, Wuhan 430077, China; banxuan@whigg.ac.cn (X.B.); lixiaodong@whigg.ac.cn (X.L.); zhangyihang12@us.ac.cn (Y.Z.); duyun@whigg.ac.cn (Y.D.)

² School of Geography, University of Nottingham, University Park, Nottingham NG7 2RD, UK; Giles.Foody@nottingham.ac.uk

³ Yangtze River Fisheries Research Institute, Chinese Academy of Fishery Science, Jingzhou 434000, China; duhao@yfi.ac.cn

* Correspondence: lingf@whigg.ac.cn; Tel.: +86-27-6888-1901

Received: 19 September 2017; Accepted: 14 November 2017; Published: 16 November 2017

Abstract: Dams play a significant role in altering the spatial pattern of temperature in rivers and contribute to thermal pollution, which greatly affects the river aquatic ecosystems. Understanding the temporal and spatial variation of thermal pollution caused by dams is important to prevent or mitigate its harmful effect. Assessments based on in-situ measurements are often limited in practice because of the inaccessibility of water temperature records and the scarcity of gauges along rivers. By contrast, thermal infrared remote sensing provides an alternative approach to monitor thermal pollution downstream of dams in large rivers, because it can cover a large area and observe the same zone repeatedly. In this study, Landsat Enhanced Thematic Mapper Plus (ETM+) thermal infrared imagery were applied to assess the thermal pollution caused by two dams, the Geheyan Dam and the Gaobazhou Dam, located on the Qingjiang River, a tributary of the Yangtze River downstream of the Three Gorges Reservoir in Central China. The spatial and temporal characteristics of thermal pollution were analyzed with water temperatures estimated from 54 cloud-free Landsat ETM+ scenes acquired in the period from 2000 to 2014. The results show that water temperatures downstream of both dams are much cooler than those upstream of both dams in summer, and the water temperature remains stable along the river in winter, showing evident characteristic of the thermal pollution caused by dams. The area affected by the Geheyan Dam reaches beyond 20 km along the downstream river, and that affected by the Gaobazhou Dam extends beyond the point where the Qingjiang River enters the Yangtze River. Considering the long time series and global coverage of Landsat ETM+ imagery, the proposed technique in the current study provides a promising method for globally monitoring the thermal pollution caused by dams in large rivers.

Keywords: dam; thermal pollution; remote sensing; Landsat; water temperature; thermal infrared image

1. Introduction

Water temperature is an important physical property of rivers because it has significant effects on many economic and ecological aspects [1–4]. Water temperature affects water quality, such as dissolved oxygen and suspended sediment concentration. It is one of the most critical parameters that controls the overall health of aquatic ecosystems in rivers, and also has considerable influence on the growth rate and spatial distribution of aquatic organisms. Moreover, water temperature is

economically important because of its influence on water requirements for industry and aquaculture. Water temperature variation in rivers is hard to quantify in practice, because it is typically spatially and temporally heterogeneous [5]. Generally, river water temperature is affected by many factors, such as atmospheric conditions, topography and stream discharge [2]. The change of natural conditions, such as global climate change, affects the pattern of river water temperature [6]. Besides, river water temperature is also greatly affected by human activities, such as riparian land cover change and effluent point discharges from power stations [2].

Building dams along rivers is one of the most important human activities that change the hydrological processes in rivers [7–9]. Specifically, river water temperature is often altered by dams. The impact of an upstream reservoir on downstream river water temperature primarily depends on its thermal stratification characteristics, and design and operation mode [10,11]. In a reservoir, thermal stratification is common in summer, because the upper layers of water are warmed by solar radiation and cooler waters remain underneath in the hypolimnion. In the winter, however, the upper layer temperatures often are cooled and the thermal stratification reduces and may disappear because of full vertical mixing. Therefore, water temperatures downstream dams may be substantially changed by the reservoir released water at different temperatures. Dam-induced modifications to a river's thermal regime can lead to unprecedented ecological and environmental results for the river downstream. This abrupt thermal shift phenomenon is then often referred as "thermal pollution", because it tends to bring harmful consequences to freshwater ecosystems [10,12–14]. Analyzing the spatial and temporal variation pattern of water temperature downstream of dams caused by thermal pollution is therefore important for reservoir management to prevent or mitigate thermal pollution using optimized operations.

Thermal pollution attributed to dams is typically analyzed with in-situ measured water temperature records [10]. By measuring water temperatures using a network of in-stream gauges, the magnitude, and the spatial and temporal patterns of thermal pollution caused by a dam can be studied. This technique can provide favorable results if long-term downstream temperature records measured by a dense observation network are available. In practice, however, long time temperature records are not always existent or available to the public in many areas. Moreover, in-situ gauges are often sparsely distributed in rivers, and using data measured in only one or several gauges cannot provide adequate information on the spatial distribution of water temperature.

Compared with in-situ measurements, thermal infrared remote sensing technique provides an attractive alternative for measuring water temperatures and quantifying spatial patterns of water temperature at multiple spatial scales [15]. For example, coarse spatial resolution imagery, such as Moderate Resolution Imaging Spectroradiometer (MODIS), have been widely used to map the spatial and temporal patterns of temperature in large lakes and reservoirs [16,17]. Medium spatial resolution satellite imagery, such as Landsat thermal infrared imagery, have been used to quantify the longitudinal and temporal thermal patterns along rivers [18], and to identify the groundwater contribution [19]. Fine spatial resolution airborne thermal infrared imagery is becoming popular for the accurate measurement of water temperatures for small water bodies [5,20–25].

The Landsat Enhanced Thematic Mapper Plus (ETM+) sensor, which has a thermal infrared band with a 60 m spatial resolution and has a large amount of data archived from 1999 available free to public, provides a promising means to quantify water thermal variability [15,26–30]. Compared with coarse spatial resolution remote sensing imagery, such as MODIS, which is unsuitable for river applications due to its coarse spatial resolution, Landsat ETM+ satellite thermal infrared imagery have a finer spatial resolution and can be used to accurately estimate water temperatures in rivers. Compared with airborne thermal infrared remote sensing imagery, using Landsat ETM+ satellite thermal infrared imagery also has its potential advantages. Both the spatial and temporal coverage achievable with airborne remote sensing are always limited, and only a few thermal infrared images within small areas can be used in most cases, while Landsat ETM+ satellite imagery has a long period global coverage.

The primary objective of the current research is to investigate the capability of a long series of Landsat ETM+ satellite thermal infrared images to assess the thermal pollution caused by dams. We investigate

the temperature estimation method for Landsat ETM+ imagery and analyze the uncertainty of result caused by imperfect atmospheric correction. The spatio-temporal pattern of thermal pollution caused by two dams in the study area is then analyzed with estimated river water temperatures. The potential applications and limitations of the proposed approach are also discussed. The contributions of this research are twofold. First, to our knowledge, it is the first time that the thermal pollution caused by dams is assessed by using satellite remote sensing technology. Second, a spatio-temporal analysis method is proposed in order to decrease the uncertainty of data provided by satellite images.

2. Materials and Methods

2.1. Study Area

The study focused on the Qingjiang River, a first-order tributary of the Yangtze River downstream of the Three Gorges Reservoir in Hubei Province, Central China. The Qingjiang River has a watershed area of approximately 17,000 km², with the mainstream having a total length of 423 km. A cascade of reservoirs can be found along the Qingjiang River. The study area ranges from the upstream Geheyan reservoir to the river mouth, including the Geheyan and Gaobazhou Dams that were constructed in 1994 and 2000, respectively (Figure 1). The monthly mean air and water temperatures measured in the Yichang hydrology station (Figure 1) in the period 2000–2004 are shown in Figure 2. The mean monthly air temperature is higher than the mean monthly water temperature in summer, while, in winter, the mean monthly water temperature is higher than the mean monthly air temperature.

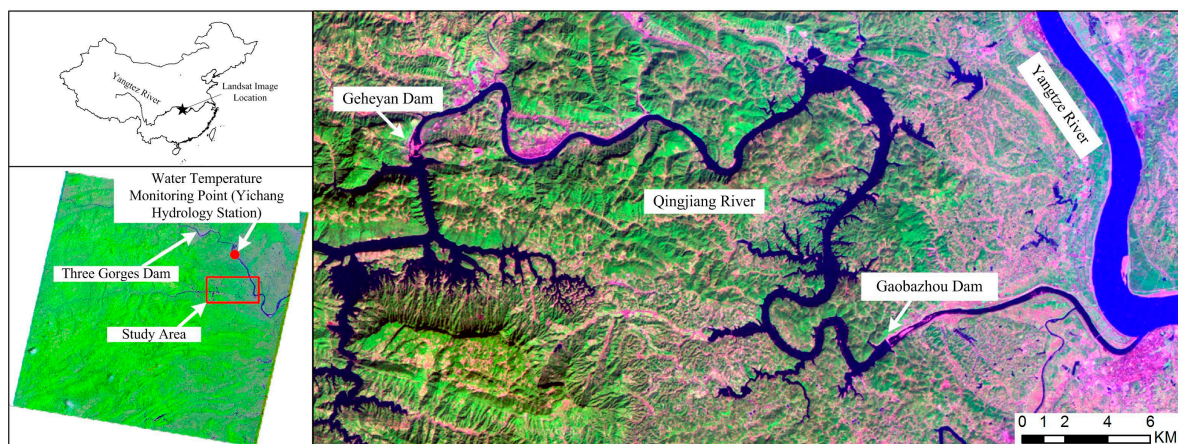


Figure 1. Study area (Qingjiang River watershed in central China) and locations of dams analyzed in this study.

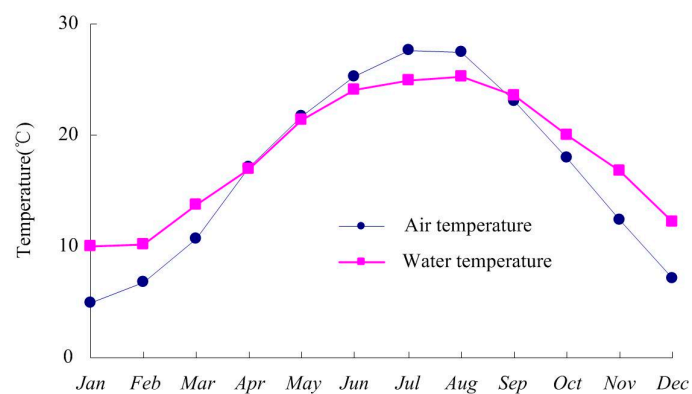


Figure 2. Mean monthly air and water temperatures of the Yichang hydrology station in the period 2000–2004.

The distance between the Geheyan and Gaobazhou Dams is approximately 50 km, and the distance between the Gaobazhou Dam and the river mouth into the Yangtze River is approximately 12 km. The river width in the study area is typically between 200 and 500 m. The normal water level of the Geheyan reservoir is about 200 m, while the normal water level of the Gaobazhou reservoir is about 80 m. The monthly mean discharges of both reservoirs in the period 2000 to 2004 are shown in Figure 3, and the annual flow discharges in this period are 400 m³/s and 436 m³/s, respectively.

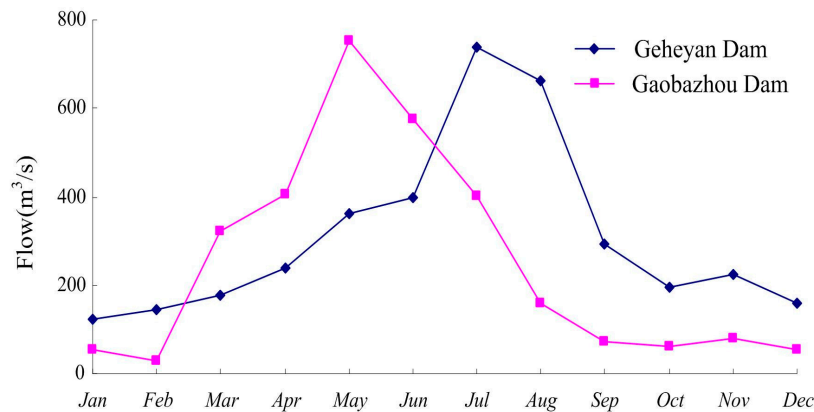


Figure 3. Mean monthly flows in the Geheyan and Gaobazhou Dams in the period 2000–2004.

Figure 4 shows the change of water temperature with the water depth in various seasons for the Geheyan reservoir [31]. It is shown that the water temperature distribution is stratified in the vertical domain and the pattern varies in time. In summer, for example, on 28 July 1995, the surface water temperature was higher than 30 °C. With the increase of water depth, the water temperature decreased rapidly at first. From the depths 10 to 40 m, the water temperature began to decrease slowly. However, from 40 to 50 m, the water temperature had a rapid decrease. Below the depth of 50 m, water temperature decreased slowly again. On days in other seasons, such as on 26 October 1995 and 24 April 1996, the water surface temperatures were still higher than those in the depths of 80 m. However, the water difference was only about 5–10 °C, and was much less than that in the summer, which reached 20 °C.

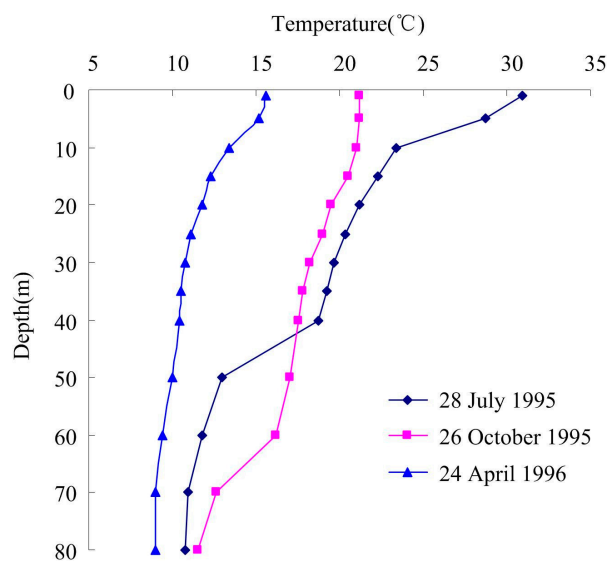


Figure 4. Vertical water temperature distribution in the Geheyan reservoir on three dates (spring, summer and autumn). The water temperature distribution is stratified in vertical dimension and the pattern is different at different time.

2.2. Landsat Imagery and Processing

The primary data source was a series of Landsat-7 ETM+ satellite images. The spatial resolution of the thermal infrared band (10.45 to 12.5 μm) for the ETM+ is 60 m \times 60 m; other bands (1, 2, 3, 4, 5 and 7) for ETM+ have a spatial resolution of 30 m. The selected Landsat scene was path 125/row 39, which covers the extent of the area of interest. Scenes that were mostly cloud-free from 2000 to 2014 were ordered and downloaded for free from the United States Geological Survey Earth Explorer website [32]. All images were Level 1T products, which have been precision and terrain corrected in the GeoTIFF format and are in the UTM Zone 49N projection and WGS datum. The resulting dataset comprised 54 full scenes, including 39 scan-line corrector off (SLC-off) images. In the analysis, the SLC-off data would lower the data quality and affect the result. Although the gaps caused by SLC-off appeared in different locations along the Qingjiang River, no gap filling method was used in this study to avoid the uncertainty brought by gap filling methods.

2.3. Methods

In this study, the spatio-temporal pattern of thermal pollution caused by dams was analyzed using the time series Landsat ETM+ images through the steps, as shown in Figure 5, which are introduced in detail in the following sections.

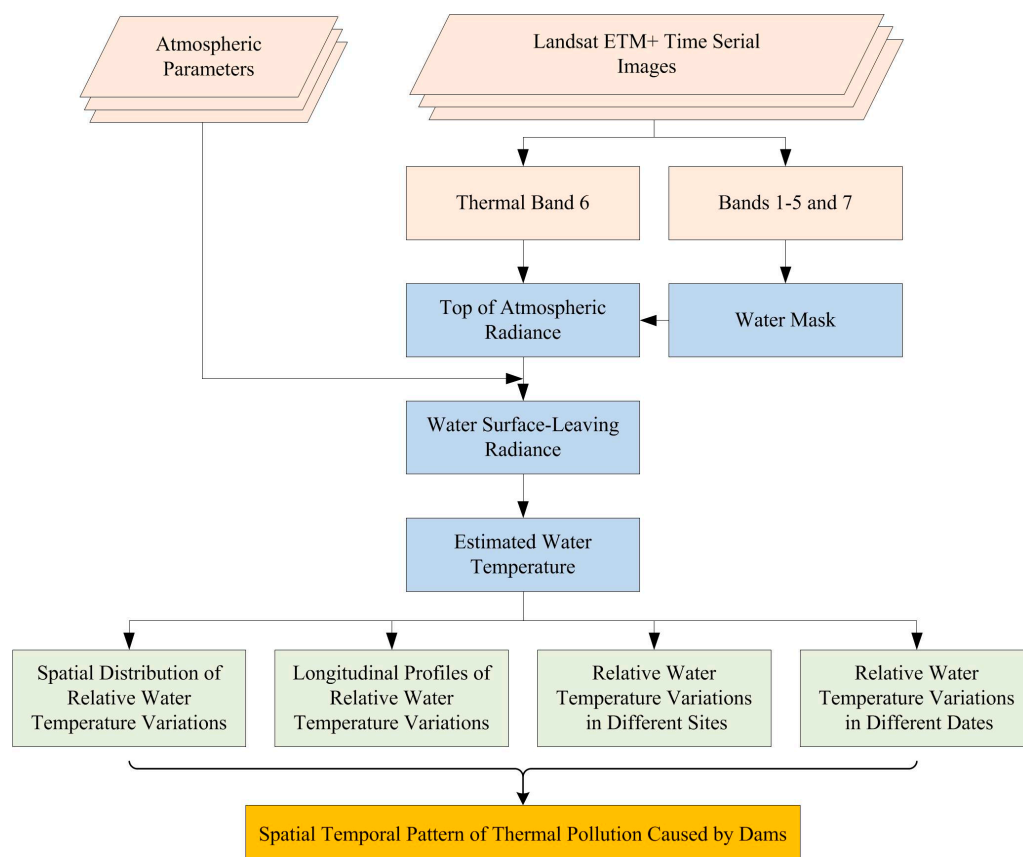


Figure 5. Flowchart for monitoring thermal pollution downstream of dams with Landsat ETM+ thermal infrared images.

2.3.1. Water Mask

First, to determine the water temperature along the river, a water mask was generated. The unsupervised Iterative Self-Organizing Data Analysis Technique (ISODATA) was applied on all six 30 m spatial resolution bands for each Landsat scene [33]. The resulting clusters were then

aggregated into a land/water classification map, which was used to create a binary water mask. Considering that the water mask has a finer spatial resolution (30 m) than the thermal band, only the coarse resolution pixels in the thermal infrared band that are fully integrated into the water mask were considered as water and were applied to determine water temperature.

2.3.2. Water Surface Temperature Estimation

Digital numbers (DN) for each water pixel in the band 6 (low gain) of Landsat ETM+ scenes were then used to derive water surface temperatures. First, digital numbers were converted to Top of Atmospheric (TOA) spectral radiance by applying the gain and bias coefficients provided along with Landsat ETM+ scenes:

$$L_{\lambda} = gain \times DN + bias. \quad (1)$$

where L_{λ} is the TOA spectral radiance at λ wavelength in $W \cdot m^2 \cdot sr \cdot mm$, DN is the digital number in the scene, and $gain$ and $bias$ are calibration parameters, and are set to be 0.067087 and -0.07 for the band 6 (low gain) of Landsat 7 ETM+ images.

Then, the TOA spectral radiance was further converted to a surface-leaving radiance by prescribing the target emissivity and removing the effect of the atmosphere, which are the most important issues for the estimation of temperature, based on the radiative transfer equation [34]. The equation used for this correction is:

$$L_{\lambda(T_s)} = \frac{L_{\lambda} - L_{\lambda}^{up}}{t \times \varepsilon_{\lambda}} - \frac{1 - \varepsilon_{\lambda}}{\varepsilon_{\lambda}} \times L_{\lambda}^{down}. \quad (2)$$

where $L_{\lambda(T_s)}$ is the corrected surface radiance, L_{λ} is the uncorrected spectral radiance calculated in Equation (1), L_{λ}^{up} is the upwelling radiance, L_{λ}^{down} is the downwelling radiance, t is the atmospheric transmissivity, and ε_{λ} is the water emissivity.

In this study, the emissivity of water was set as 0.9885 according to Simon et al. [35]. The other three parameters used in Equation (2) were obtained with the atmospheric correction tool [36] developed by Barsi et al. [34] for the TM and ETM+ thermal bands. According to the date, time, and location of the Landsat scene, the atmospheric correction parameter calculator uses the National Centers for Environmental Prediction-modeled global atmospheric profiles as input data, along with MODTRAN and other integration algorithms, to derive site-specific atmospheric transmission, upwelling atmospheric radiance and down-welling atmospheric for each given Landsat scene.

Finally, the corrected water surface radiance $L_{\lambda(T_s)}$ was then converted into water temperature by using a sensor-specific approximation to Planck's function [37]:

$$T_s = \frac{K_2}{\ln\left(\frac{K_1}{L_{\lambda(T_s)} + 1}\right)}. \quad (3)$$

where T_s is the water temperature (K). K_1 and K_2 are thermal constants, where $K_1 = 1282.71$ K and $K_2 = 666.09$ $W \cdot m^2 \cdot sr \cdot mm$ for the Landsat ETM+ sensor. With all estimated water temperature values, the spatio-temporal pattern of thermal pollution caused by both dams could be analyzed. It needs to be emphasized that no in-situ observation water temperature data are available along the Qingjiang River at present. Therefore, in this study, the thermal pollution caused by both dams is assessed using only the Landsat ETM+ images.

3. Results

3.1. Estimated Water Temperature

To validate the estimated water temperatures, the results were compared with in-situ observed water temperatures. At present, there are no water temperature observation data available in the

Qingjiang River. Therefore, the water temperature monitoring point (30°43′15″N, 111°15′47″E) located in the Yichang hydrology station in the Yangtze River within the same Landsat scene, as shown in Figure 1, were used for validation in this study. Five-year daily water temperature measured at 8:00 a.m. local time during 2000–2002 and 2007–2008 were collected. During the period, there are 24 Landsat scenes available and all measured water temperature values were then compared with corresponding estimated water temperatures, to assess the accuracy of results.

Table 1 shows the measured water temperatures (T_m), estimated water temperatures (T_e), along with all used atmosphere parameters of all validation dates. In general, the accuracy of the water temperature estimated the radiative transfer equation algorithm is high. Most estimated water temperature values are similar with measured water temperature values. However, it is also noticed that there are several larger errors in resulting water temperatures estimated from Landsat images, especially when the water temperature is high. The main reason is that the in-situ temperatures were observed at 8:00 a.m. local time, while the satellite passed the area at about 10:00 a.m. local time. In general, when the water temperature is low, for example in the winter, the difference of water temperatures between the in-situ observation time and satellite pass time is small. By contrast, when the water temperature is high, for example in the summer, such as 20 July and 5 August 2001, the difference of water temperatures between the in-situ observation time and satellite pass time is large and may be a few degrees.

Table 1. Comparison between measured water surface temperatures (T_m) and estimated water surface temperatures (T_e). dT is the temperature difference between the measured and estimated water surface temperatures.

Date	DN	T_m	t	L_{λ}^{up}	L_{λ}^{down}	T_e	dT
27 March 2000	115	13.3	0.91	0.65	1.12	14.58	1.28
28 April 2000	121	18.1	0.74	1.8	2.9	20.57	2.47
14 May 2000	130	20.6	0.7	2.35	3.8	24.79	4.19
15 June 2000	127	23	0.67	2.49	3.95	24.00	1.00
6 November 2000	121	18.1	0.84	1.16	1.92	18.68	0.58
10 February 2001	108	10.8	0.92	0.45	0.77	11.47	0.67
30 March 2001	116	16.8	0.83	1.17	1.96	16.14	−0.66
20 July 2001	127	27.1	0.39	4.67	6.7	29.99	2.89
5 August 2001	130	27	0.41	4.58	6.63	31.63	4.63
12 January 2002	123	21.8	0.87	0.85	1.43	20.51	−1.29
17 March 2002	123	22.4	0.81	1.2	2.01	21.98	−0.42
2 April 2002	106	8.4	0.63	2.73	4.24	7.26	−1.14
24 August 2002	125	21.6	0.44	4.4	6.47	24.04	2.44
25 September 2002	117	17.2	0.72	2.04	3.23	16.80	−0.40
30 December 2002	115	16.3	0.9	0.55	0.93	16.22	−0.08
2 May 2007	119	17.2	0.73	2.04	3.28	17.38	0.18
6 August 2007	127	24.2	0.46	4.25	6.24	25.77	1.57
23 September 2007	125	22.2	0.83	1.25	2.07	21.14	−1.06
9 October 2007	123	21.8	0.81	1.26	2.05	21.41	−0.39
25 October 2007	123	22.4	0.76	1.69	2.71	21.34	−1.06
14 February 2008	106	10.4	0.95	0.26	0.45	10.02	−0.38
21 May 2008	125	21.6	0.85	1.17	1.96	20.31	−1.29
28 November 2008	117	17.2	0.94	0.34	0.6	16.48	−0.72
14 December 2008	115	16.3	0.93	0.41	0.69	15.38	−0.92

Figure 6 shows the plot of estimated water surface temperature and measured water surface temperature. Most scatter points are located near the 1:1 line. The correlation coefficient is 0.9268, and the root mean squared error (RMSE) is 1.07 °C, showing the effectiveness of the method used to estimate water temperature from the Landsat ETM+ thermal band.

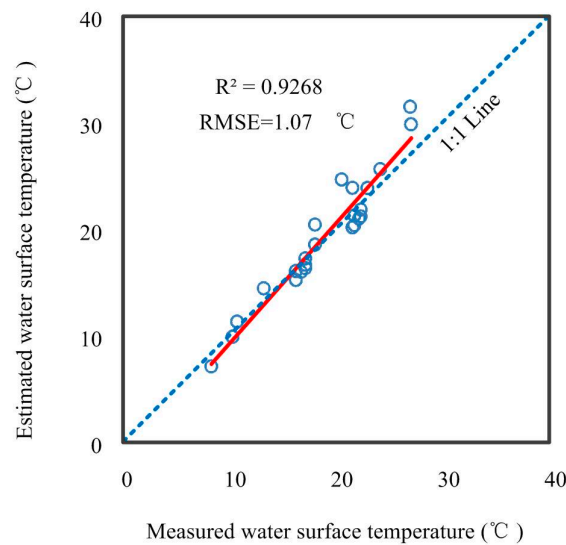


Figure 6. Plot of estimated water surface temperature versus measured water surface temperature.

3.2. Uncertainty Analysis of Water Temperature Estimation

The objective of the study is to analyze the dam-caused thermal pollution, which is mainly represented by the water temperature variation downstream of the dam. The temperature difference (or relative temperature) between water bodies below the dam and in the reservoir upstream may be more informative than absolute water temperatures. Therefore, besides direct temperature comparison, an uncertainty analysis was further performed. The uncertainty analysis pays no attention to absolute water temperatures themselves, but the water temperature difference between two sites in the same Landsat scene.

In the analysis of the uncertainty of temperature differences, two water points in the Landsat scene were first selected. The water temperatures of both points were estimated using the original downloaded atmosphere parameters, and their water temperature difference was also calculated. Then, random errors were added to original downloaded atmosphere parameters (L_{λ}^{up} , L_{λ}^{down} , and t) in Equation (2) to obtain simulated atmosphere parameters. Water temperatures of both points were again estimated with simulated atmosphere parameters and their water temperature difference was calculated. Finally, error between water temperatures of one point estimated with original atmosphere parameters and simulated atmosphere parameters, and error between water temperature differences of two points estimated with original atmosphere parameters and simulated atmosphere parameters, are compared, in order to assess the uncertainty of the water temperature difference caused by the uncertainty of used atmosphere parameters.

Table 2 shows the results of uncertainty analysis. Here, the difference of DN values between two selected water points is 10, which is larger than most DN difference values between two water points in all Landsat scenes in the study area. The error of atmosphere parameters is set to be in the range of -50% to 50% . With these simulated atmosphere parameters, the absolute error of estimated water surface temperatures can reach to $50\text{ }^{\circ}\text{C}$, which is not practical. Therefore, only absolute errors of estimated water surface temperatures based on simulated atmosphere parameters within the range between $[-9\text{ }^{\circ}\text{C}, 9\text{ }^{\circ}\text{C}]$ are considered. It is noticed that, in most cases, the RMSE value of estimated temperature difference between two sites is only about $1\text{ }^{\circ}\text{C}$, even the error of estimated absolute temperature of each site is larger than $7\text{ }^{\circ}\text{C}$. Given water temperatures estimated from the Landsat ETM+ images already have a high accuracy as the validation result shows, the water temperature difference, which is more important for thermal pollution assessment, can also be estimated with a high accuracy for each Landsat ETM+ scene in the study area.

Table 2. Uncertainty analysis for the relative temperature difference. $E1$ is the error between absolute water temperatures of one point estimated with original atmosphere parameters and simulated atmosphere parameters. $E2$ is the error between water temperature differences of two points estimated with original atmosphere parameters and simulated atmosphere parameters.

Range of $E1$	$E2$	
	Mean	RMSE
[−9 °C, −7 °C]	−0.01 °C	1.01 °C
[−7 °C, −5 °C]	−0.08 °C	0.95 °C
[−5 °C, −3 °C]	−0.13 °C	1.13 °C
[−3 °C, −1 °C]	0.03 °C	0.83 °C
[−1 °C, 1 °C]	−0.04 °C	0.93 °C
[1 °C, 3 °C]	0.05 °C	1.02 °C
[3 °C, 5 °C]	−0.01 °C	0.85 °C
[5 °C, 7 °C]	0.12 °C	0.93 °C
[7 °C, 9 °C]	0.10 °C	0.82 °C

3.3. Spatio-Temporal Variation of Thermal Pollution

Figure 7 shows the resulting relative water temperature variations over four different dates. The thermal pollution is clearly shown in Figure 7. In summer scenes of both years, generally, river temperatures were warmer upstream and cooler downstream for both dams. For example, in the scene of 17 July 2000, water temperature is warm in the reservoir upstream of the Geheyan Dam. Downstream of the dam, water temperature cools along the river. From 30 km away from the dam to the reservoir upstream of the Gaobazhou Dam, the water temperature warms again. Downstream of the Gaobazhou Dam, however, water temperature becomes cooler until the water flows into the Yangtze River. Moreover, it is also noticed that the spatial pattern of relative water temperature variations is different in the two summer days in the years 2000 and 2001. In winter, by contrast, there are only slightly water temperature variations along the river, and the abrupt thermal shift is unnoticeable for both dams.

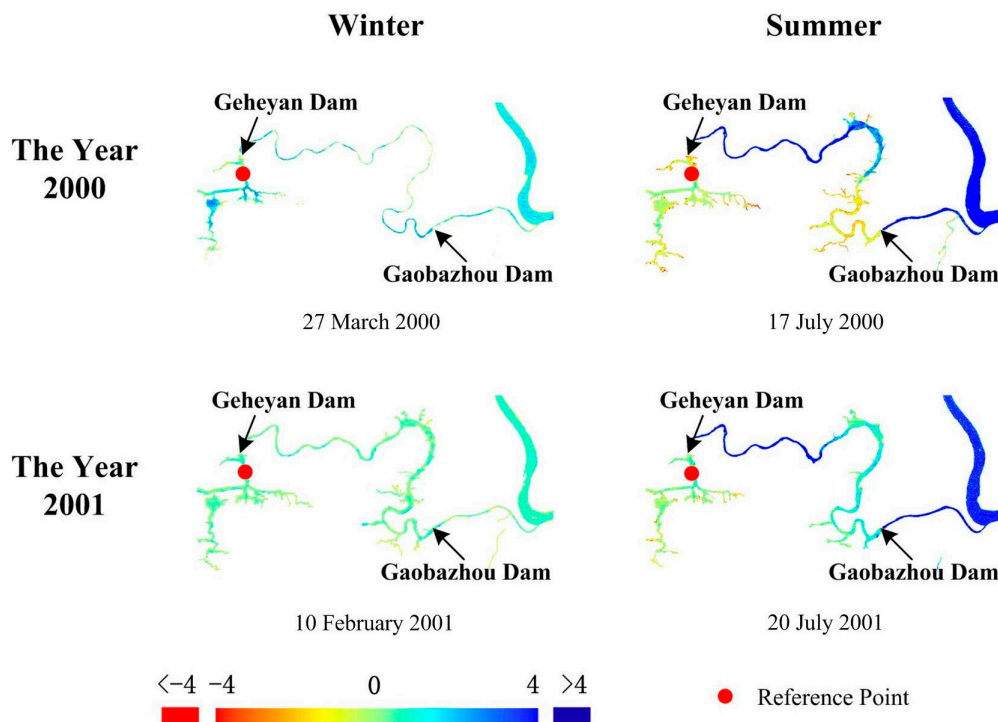


Figure 7. Relative water temperature variations derived using Landsat ETM+ imagery over four different dates.

Figure 8 shows longitudinal profiles of relative water temperatures from the reservoir upstream of the Geheyan Dam to the river mouth in four different dates. Discontinuities of relative water temperatures are clearly visible at the reservoir locations, in July 2000 and 2001. The longitudinal relative water temperature profile shows a general pattern of “warm, cool, warm, and cool”. Taking the result on 20 July 2001 as an example, relative water temperatures in the reservoir upstream of the Geheyan Dam are approximately $0\text{ }^{\circ}\text{C}$, meaning that open water bodies in the reservoir almost have the same water temperatures. A rapid temperature decrease is noticeable below the Geheyan Dam, where the relative water temperature reaches approximately $-5\text{ }^{\circ}\text{C}$. In the range of 0 km to 25 km downstream the dam, the relative water temperature remains stable. Beyond this area, the relative water temperature increases rapidly until 35 km downstream of the dam, again reaching approximately $0\text{ }^{\circ}\text{C}$ and remains stable until the Gaobazhou Dam is reached. The relative water temperature again decreases to about $-5\text{ }^{\circ}\text{C}$ downstream of the Gaobazhou Dam, remaining stable until the river enters the Yangtze River. In 17 July 2000, a general trend exists, although the profile also shows changes in the longitudinal heating rate along the river gradient. In the winter, such as that on 27 March 2000 and 10 February 2001, the relative water temperature profiles are much different with those in summer. The relative water temperatures generally keep near zero, meaning that water temperatures up and downstream both dams are similar.

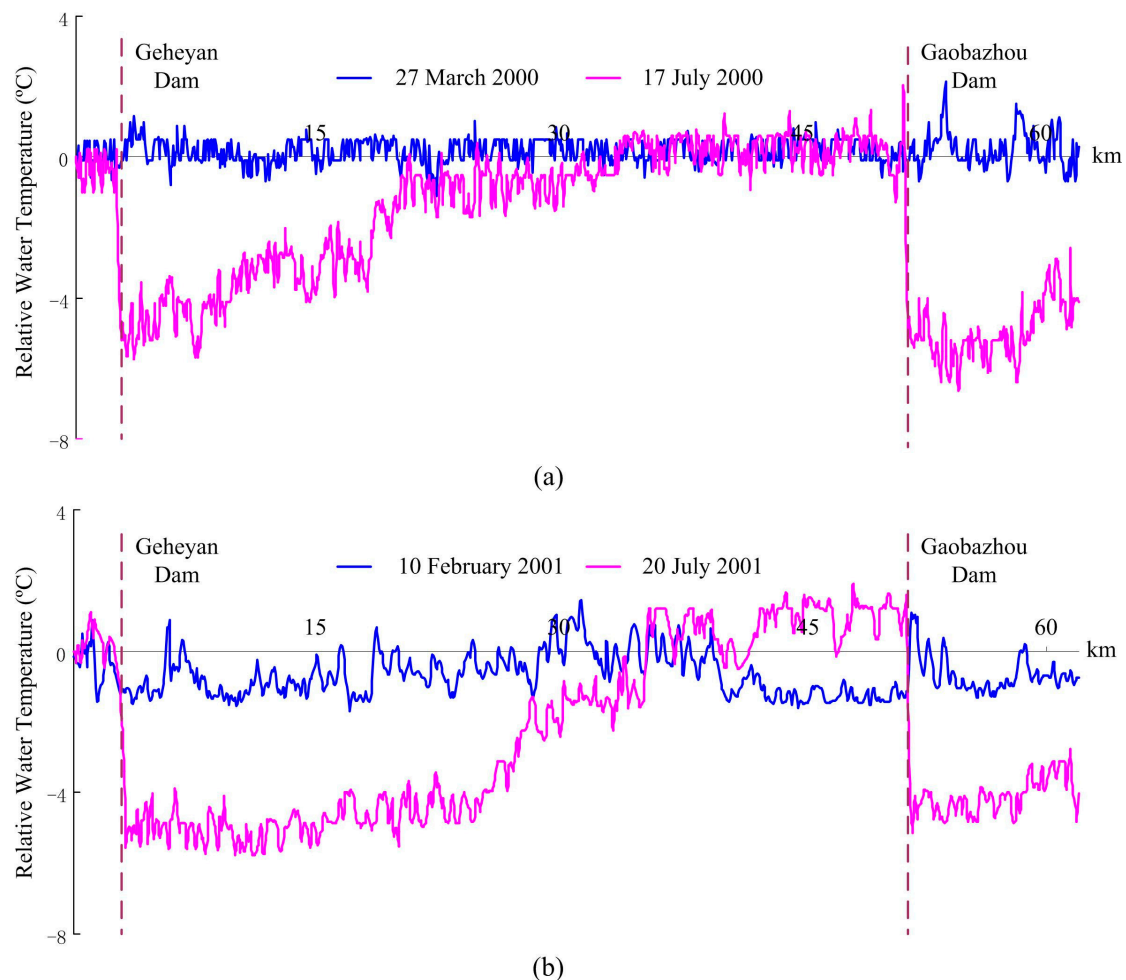


Figure 8. Longitudinal profiles of relative water temperatures from the reservoir upstream of the Geheyan Dam to the river mouth over different times.

Water temperature values in four different sites, including the Geheyan reservoir, the site located 1 km away from the Geheyan Dam, the Gabazhou reservoir, and the site located 1 km away from the

Gabazhou Dam, are plotted in Figure 9. It is noted that the intra-annual change of water temperatures in the four sites are mainly affected by the meteorological conditions, and the trends of the water temperature measured by Landsat ETM+ images are similar with that of the in-situ measurements, as shown in Figure 2. However, for both dams, water temperatures upstream of the dams vary within a larger range than downstream of the dams. A paired sample *t*-test showed that, at the 5% level, there are significant differences between water temperature of the Geheyan reservoir and water temperatures of the sites located 1 km downstream of the Geheyan Dam. The water temperature of the Gaobazhou reservoir was also found to have a significant difference with water temperatures of the site located 1 km downstream of the Gaobazhou Dam, at the 5% level. However, no significant differences were found between water temperature of the Geheyan reservoir and those of the Gaobazhou reservoir.

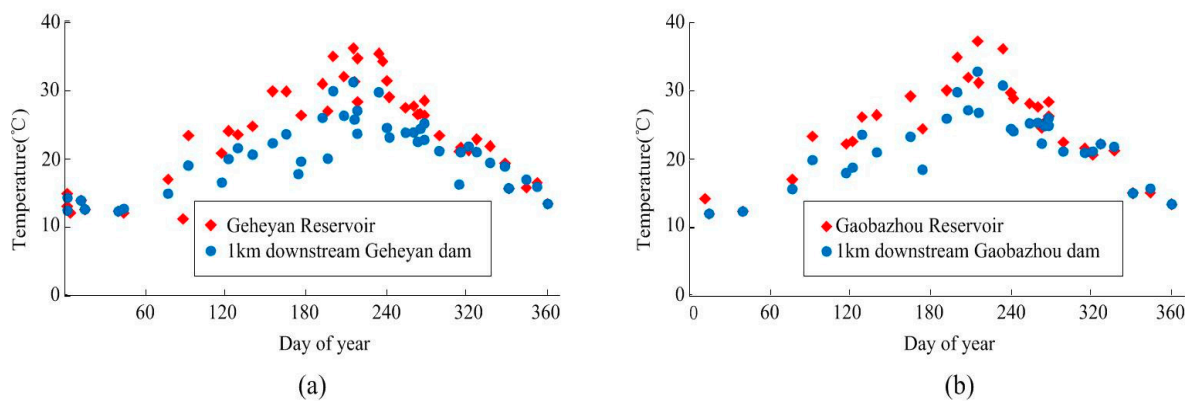


Figure 9. (a) Water temperatures in the Geheyan reservoir and 1 km downstream of the Geheyan Dam; (b) Water temperatures in the Gaobazhou reservoir and 1 km downstream of the Gaobazhou Dam. Note that the number of water temperature values in each case is different because of the SLC-off problem of Landsat ETM+ images.

Figure 10 shows the differences between water temperatures upstream the dams and water temperatures downstream the dams in different sites along the river. Figure 10a–e shows the results of the sites located 1, 10, 20, 30, and 50 km away from the Geheyan Dam, respectively. Similarly, Figure 10f–h shows water temperature differences of the different sites located 1, 5, and 10 km downstream of the Gabazhou Dam, respectively, by comparing the reference water and those of the study locations. In Figure 10a–f, both Geheyan and Gaobazhou Dams have noticeable effects on water temperature below the dams. The trends of water temperature difference are similar for both dams, although the difference in the Geheyan Dam seems slightly larger. Generally, water temperatures below the dams are lower than that of the reservoir in the summer. The highest difference exceeds 5 °C for both dams. By contrast, the water temperature difference is small in winter. Meanwhile, the effect of the dam on downstream water temperatures is observed to decrease with increasing distance to the Geheyan Dam. Comparing the sites 20, 10, and 1 km downstream of the Geheyan Dam, the effect trend is similar, whereas the amplitude is decreasing. In the sites 30 and 50 km downstream of the Geheyan Dam, as shown in Figure 10d,e, noticeable trends of water temperature differences are essentially nonexistent, and the deviation indeed results from other factors, such as the uncertainty of water temperature extracted by Landsat images. The trend for the Gaobazhou Dam is similar, that is, the amplitude decreases with increasing distance. Considering that the Qingjiang River flows into the Yangtze River in the site 12 km downstream of the Gaobazhou Dam, the Gaobazhou Dam also has important effect on the thermal pattern in the main channel of the Yangtze River.

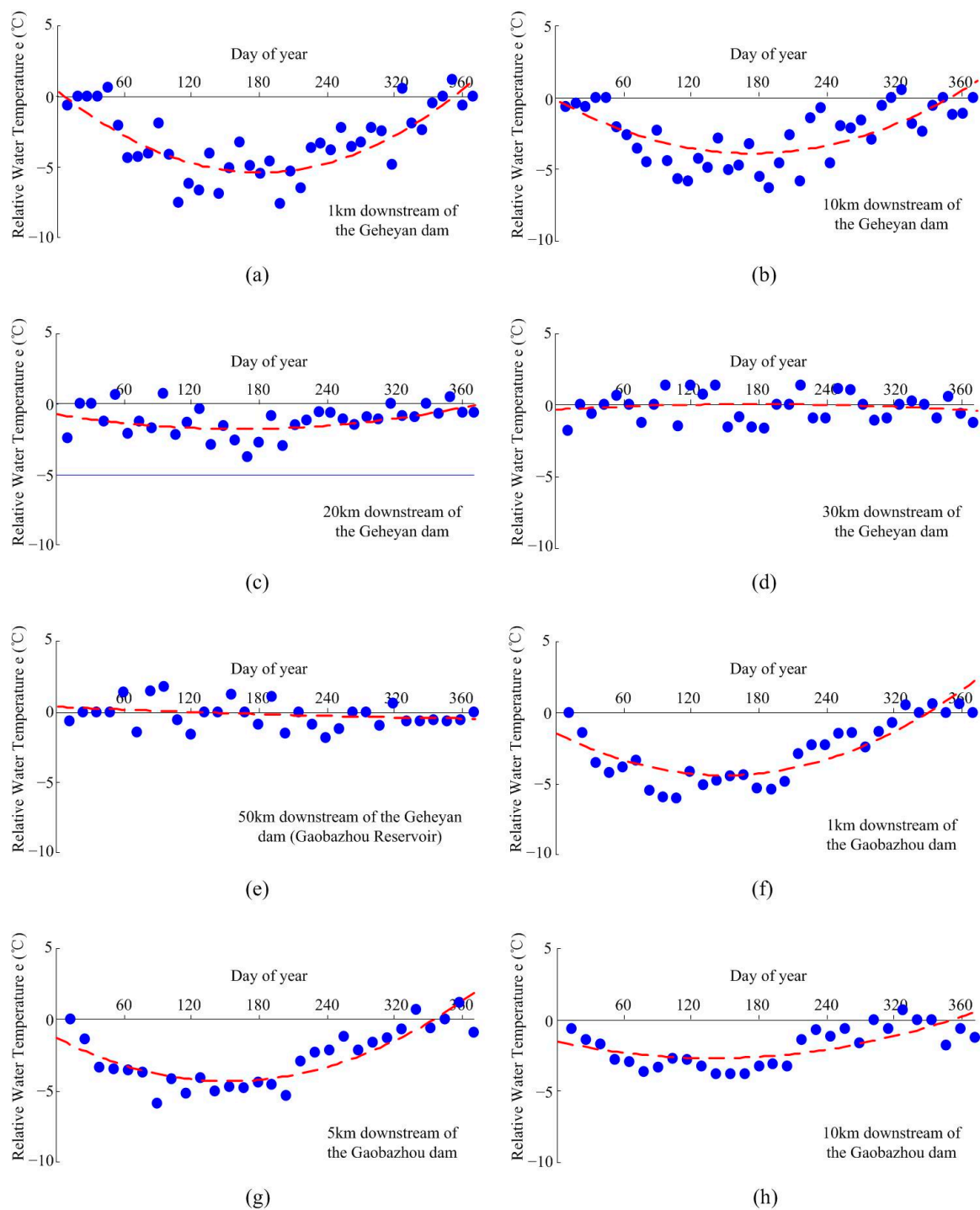


Figure 10. Relative water temperatures in different sites: (a–e) relative water temperatures of downstream sites with different distances to the Geheyuan Dam; and (f–h) relative water temperatures of downstream sites with different distances to the Gaobazhou Dam.

4. Discussion

Thermal pollution caused by dams has an important impact on the downstream river environment and ecology. The popular method of using long term in-situ water temperature records to evaluate this influence is limited because in-situ records are not available for many areas. More importantly, in-situ records are always measured only at sparse certain locations, and cannot provide detailed

spatial information for thermal pollution assessment. By contrast, Landsat ETM+ thermal infrared imagery can provide long term spatially continuous water temperatures, and then could be used as an alternative dataset to assess the thermal pollution for large rivers.

By analyzing the spatial and temporal pattern of water temperatures estimated by Landsat ETM+ thermal infrared images, it is shown that both Geheyan and Gaobazhou Dams have a significant effect on river temperature. Both Geheyan and Gaobazhou Dams are used for hydropower generation, then the water is then taken from deep in the reservoir and after use is discharged downstream of the dam. In Figure 4, it is shown that the water temperature distribution in the Geheyan reservoir is stratified in the vertical dimension. In summer, the deep water is much cooler than the surface water. Then, the released water from the reservoir to the downstream river is much cooler than the water in the river, making the water temperature downstream of Geheyan Dam much lower than the surface water temperature in the Geheyan reservoir. In spring and autumn, although the deep water in the reservoir is still cooler than the surface water, the water temperature difference is much less than that in the summer. Moreover, as shown in Figure 3, the monthly mean discharges in spring and autumn are also much less than those in summer. Then, the temperature different between surface water in the reservoir and that in the river downstream the dam is less than that in summer. The phenomenon is in accordance with a typical thermal pollution caused by dams, due to the thermal stratification characteristics of the reservoir formed by dams.

In this study, the inter-annual variation of water temperatures caused by meteorological and hydrological conditions are not considered. The main reason is that, although the satellite can revisit the same area every 16 days, only several Landsat ETM+ images can be applied to estimated water temperatures each year because of the problem of cloud coverage. Then, all available Landsat ETM+ imagery is combined to analyze the intra-annual water temperature variations. In Figures 9 and 10, it is noticed that both absolute and relative water temperatures are dissimilar for different dates and locations. In general, the magnitude of thermal alterations caused by dams in summer is larger than that in winter. However, the magnitude of thermal alterations might be different in the same season. For example, in Figure 10b, near the 240th day, one relative water temperature value is about -5°C and another value is about 0°C . This is mainly caused by different meteorological and hydrological conditions in these two days. In general, with all available datasets, the general trend of thermal pollution caused by both dams can be acquired, but detailed information of the daily thermal pollution pattern cannot be assessed if using only Landsat ETM+ images.

The effectiveness of the proposed method is mainly affected by the accuracy of water temperatures estimated from Landsat ETM+ thermal infrared images. In practice, there are many different sources of uncertainty in river water temperature estimation [15]. The two most important influence factors, the spatial resolution of image and the water temperature estimation algorithm used, should, therefore, be carefully considered in future studies.

The spatial resolution of thermal imagery is a crucial factor that affects the accuracy of the estimated water temperature from thermal imagery. In general, in order to estimate river water temperature accurately, the rivers should be as large as three pixels in the thermal infrared imagery [15]. However, if image sharpening methods are applied, water temperatures in the rivers narrower than the pixel size may also be estimated, and used to identify the along-stream temperature pattern [21]. In our experiments, the river is mostly wider than 200 m. Then, Landsat ETM+ thermal images, which have a spatial resolution of 60 m, are suitable to be applied to estimate the water temperature. In other cases, if Landsat 5 TM thermal imagery with a spatial resolution of 120 m or the Landsat 8 thermal imagery with a spatial resolution of 100 m, are used, or the river width is not large enough, these advanced water temperature algorithms should be used to improve the accuracy of results [38].

Another important issue is the temperature estimation algorithm. For Landsat ETM+ imagery, only the mono-window algorithm can be applied to estimate temperature because only one thermal infrared band exists. The results in this study show that the radiative transfer equation method obtained water temperatures with a high accuracy, satisfying the need for thermal pollution analysis.

Moreover, the uncertainty analysis results show that the radiative transfer equation method can obtain temperature differences with a high accuracy even the estimated absolute water temperatures have large errors, showing the reliability of water temperature estimation with Landsat ETM+ thermal images. In practice, however, the uncertainty of estimated water surface temperature is unavoidable, because of the imperfect atmospheric correction. One possible method to reduce the impact caused by the uncertainty is using Landsat time series. For example, in this study, 54 Landsat ETM+ scenes were used. A large number of observations can help make the results robust.

In this study, Landsat ETM+ imagery are used as the only datasets to analyze the spatial temporal pattern of thermal pollution below dams. In practice, if other additional data are available, they can be incorporated into the analysis to further improve the results. For example, if in-situ water temperature records can be collected, they should be used to improve the water temperature estimation accuracy and provide more information about the thermal pollution pattern [5]. Other datasets, such as high spatial resolution airborne thermal infrared dataset, can also be fused with long term Landsat ETM+ imagery to improve the accuracy of results. Results produced by water temperature simulation models and results obtained by the current study are obviously mutually benefit, and the integration between them needs further investigation [22].

Generally, the technique presented in this study offers a useful tool to fill in the sparse in-situ observational record of water temperature in rivers. This technique can be applied in the global scale because of the long time series and global coverage of Landsat ETM+ imagery. Based on the current study, analyzing the spatial patterns of thermal pollution caused by different dams is now possible. Such an analysis is important in reservoir management. Moreover, this technique can be used to compare the effects of the various larger dams with freely available data. The approach of the current study can be easily applied in other dams located in large rivers, and the results can provide useful information for further understanding the extent and magnitude of thermal pollution associated with dams.

5. Conclusions

In this paper, we proposed a method to monitor thermal pollution below dams using long time series Landsat ETM+ thermal infrared imagery. Taking Geheyan and Gaobazhou Dams located in the Qingjiang River as a case study, water surface temperatures were estimated from 54 Landsat ETM+ thermal images. Validation and uncertainty analysis results show that the estimated water surface temperatures have a high accuracy and can be applied to analyze the spatial and temporal pattern of thermal variations resulting from the dams. The results show that, on Qingjiang River, the Geheyan and Gaobazhou Dams greatly alter the downstream water temperatures. According to the operating mode, the discharges of both dams are taken from deep in the reservoir. Due to the thermal stratification characteristics of reservoirs, the temperature difference between the released water and the surface water is then large in summer and small in winter. Moreover, the flow discharges in summer are larger than those in winter. Therefore, both dams result in a typical thermal pollution phenomenon. In summer, water temperatures downstream of both dams are cooler than those upstream of both dams, and the water temperature difference exceeds 5 °C. In winter, the water temperature remains stable along the river. The area affected by the Geheyan Dam reaches beyond 20 km along the downstream river, and that affected by the Gaobazhou Dam extends beyond the point where the Qingjiang River enters the Yangtze River.

The results show that long term Landsat ETM+ thermal infrared imagery is a useful dataset to study the river thermal behavior and to assess the thermal pollution caused by dams in large rivers. However, other possibilities for improvement should still be considered. For example, given that Landsat ETM+ images have a global coverage, the proposed method should be applied in other dams globally to assess its ability. The water temperatures estimated from Landsat ETM+ images should be compared with more in-situ observed data in different areas to assess the uncertainty of

results. Moreover, the results should be further explored with methods in other research fields, such as aquatic ecology.

Acknowledgments: This research was supported in part by the Youth Innovation Promotion Association CAS (Grant No. 2017384), and in part by the Natural Science Foundation of China (Grant No. 51479186 and No. 31772854).

Author Contributions: Feng Ling, Giles M. Foody and Yun Du conceived of the main idea and designed the experiments. Hao Du, Xuan Ban performed the experiments. Xiaodong Li and Yihang Zhang analyzed the data. The manuscript was written by Feng Ling and was improved by the contributions of all of the co-authors.

Conflicts of Interest: The authors declare no conflict of interest.

References

1. Sinokrot, B.A.; Stefan, H.G. Stream temperature dynamics—Measurements and modeling. *Water Resour. Res.* **1993**, *29*, 2299–2312. [[CrossRef](#)]
2. Caissie, D. The thermal regime of rivers: A review. *Freshw. Biol.* **2006**, *51*, 1389–1406. [[CrossRef](#)]
3. Webb, B.W.; Hannah, D.M.; Moore, R.D.; Brown, L.E.; Nobilis, F. Recent advances in stream and river temperature research. *Hydrol. Process.* **2008**, *22*, 902–918. [[CrossRef](#)]
4. Yang, D.Q.; Liu, B.Z.; Ye, B.S. Stream temperature changes over Lena River basin in Siberia. *Geophys. Res. Lett.* **2005**, *32*, L05401. [[CrossRef](#)]
5. Vatland, S.J.; Gresswell, R.E.; Poole, G.C. Quantifying stream thermal regimes at multiple scales: Combining thermal infrared imagery and stationary stream temperature data in a novel modeling framework. *Water Resour. Res.* **2015**, *51*, 31–46. [[CrossRef](#)]
6. Isaak, D.J.; Luce, C.H.; Rieman, B.E.; Nagel, D.E.; Peterson, E.E.; Horan, D.L.; Parkes, S.; Chandler, G.L. Effects of climate change and wildfire on stream temperatures and salmonid thermal habitat in a mountain river network. *Ecol. Appl.* **2010**, *20*, 1350–1371. [[CrossRef](#)] [[PubMed](#)]
7. Scarrott, R.M.J.; Reed, D.W.; Bayliss, A.C. Indexing the attenuation effect attributable to reservoirs and lakes. In *Statistical Procedures for Flood Frequency Estimation*; Flood Estimation Handbook; Robson, A., Reed, D., Eds.; Centre for Ecology & Hydrology: Wallingford, UK, 1999; Volume 5, pp. 19–26.
8. Montaldo, N.; Mancini, M.; Rosso, R. Flood hydrograph attenuation induced by a reservoir system: Analysis with a distributed rainfall-runoff model. *Hydrol. Process.* **2004**, *18*, 545–563. [[CrossRef](#)]
9. Gioia, A. Reservoir routing on double-peak design flood. *Water* **2016**, *8*, 553. [[CrossRef](#)]
10. Olden, J.D.; Naiman, R.J. Incorporating thermal regimes into environmental flows assessments: Modifying dam operations to restore freshwater ecosystem integrity. *Freshw. Biol.* **2010**, *55*, 86–107. [[CrossRef](#)]
11. Sullivan, A.B.; Rounds, S. *Modeling Streamflow and Water Temperature in the North Santiam and Santiam Rivers, Oregon, 2001-02*; US Department of the Interior, US Geological Survey: Portland, OR, USA, 2004.
12. Angilletta, M.J.; Steel, E.A.; Bartz, K.K.; Kingsolver, J.G.; Scheuerell, M.D.; Beckman, B.R.; Crozier, L.G. Big dams and salmon evolution: Changes in thermal regimes and their potential evolutionary consequences. *Ecol. Appl.* **2008**, *18*, 286–299. [[CrossRef](#)] [[PubMed](#)]
13. Lowney, C.L. Stream temperature variation in regulated rivers: Evidence for a spatial pattern in daily minimum and maximum magnitudes. *Water Resour. Res.* **2000**, *36*, 2947–2955. [[CrossRef](#)]
14. Risley, J.C.; Constantz, J.; Essaid, H.; Rounds, S. Effects of upstream dams versus groundwater pumping on stream temperature under varying climate conditions. *Water Resour. Res.* **2010**, *46*, W06517. [[CrossRef](#)]
15. Handcock, R.N.; Gillespie, A.R.; Cherkauer, K.A.; Kay, J.E.; Burges, S.J.; Kampf, S.K. Accuracy and uncertainty of thermal-infrared remote sensing of stream temperatures at multiple spatial scales. *Remote Sens. Environ.* **2006**, *100*, 427–440. [[CrossRef](#)]
16. Reinart, A.; Reinhold, M. Mapping surface temperature in large lakes with MODIS data. *Remote Sens. Environ.* **2008**, *112*, 603–611. [[CrossRef](#)]
17. Alcantara, E.H.; Stech, J.L.; Lorenzetti, J.A.; Bonnet, M.P.; Casamitjana, X.; Assireu, A.T.; Novo, E. Remote sensing of water surface temperature and heat flux over a tropical hydroelectric reservoir. *Remote Sens. Environ.* **2010**, *114*, 2651–2665. [[CrossRef](#)]
18. Wawrzyniak, V.; Piégay, H.; Poirel, A. Longitudinal and temporal thermal patterns of the French Rhône River using landsat ETM+ thermal infrared images. *Aquat. Sci.* **2012**, *74*, 405–414. [[CrossRef](#)]

19. Lalot, E.; Curie, F.; Wawrzyniak, V.; Baratelli, F.; Schomburgk, S.; Flipo, N.; Piegay, H.; Moatar, F. Quantification of the contribution of the Beauce groundwater aquifer to the discharge of the Loire River using thermal infrared satellite imaging. *Hydrol. Earth Syst. Sci.* **2015**, *19*, 4479–4492. [[CrossRef](#)]
20. Torgersen, C.E.; Faux, R.N.; McIntosh, B.A.; Poage, N.J.; Norton, D.J. Airborne thermal remote sensing for water temperature assessment in rivers and streams. *Remote Sens. Environ.* **2001**, *76*, 386–398. [[CrossRef](#)]
21. Cherkauer, K.A.; Burges, S.J.; Handcock, R.N.; Kay, J.E.; Kampf, S.K.; Gillespie, A.R. Assessing satellite-based and aircraft-based thermal infrared remote sensing for monitoring Pacific northwest river temperature. *J. Am. Water Resour. Assoc.* **2005**, *41*, 1149–1159. [[CrossRef](#)]
22. Cristea, N.C.; Burges, S.J. Use of thermal infrared imagery to complement monitoring and modeling of spatial stream temperatures. *J. Hydrol. Eng.* **2009**, *14*, 1080–1090. [[CrossRef](#)]
23. Schuetz, T.; Weiler, M. Quantification of localized groundwater inflow into streams using ground-based infrared thermography. *Geophys. Res. Lett.* **2011**, *38*, L03401. [[CrossRef](#)]
24. Dugdale, S.J.; Bergeron, N.E.; St-Hilaire, A. Temporal variability of thermal refuges and water temperature patterns in an Atlantic salmon river. *Remote Sens. Environ.* **2013**, *136*, 358–373. [[CrossRef](#)]
25. Crosman, E.; Vazquez-Cuervo, J.; Chin, T.M. Evaluation of the multi-scale ultra-high resolution (MUR) analysis of lake surface temperature. *Remote Sens.* **2017**, *9*. [[CrossRef](#)]
26. Kay, J.E.; Kampf, S.K.; Handcock, R.N.; Cherkauer, K.A.; Gillespie, A.R.; Burges, S.J. Accuracy of lake and stream temperatures estimated from thermal infrared images. *J. Am. Water Resour. Assoc.* **2005**, *41*, 1161–1175. [[CrossRef](#)]
27. Hook, S.J.; Chander, G.; Barsi, J.A.; Alley, R.E.; Abtahi, A.; Palluconi, F.D.; Markham, B.L.; Richards, R.C.; Schladow, S.G.; Helder, D.L. In-flight validation and recovery of water surface temperature with landsat-5 thermal infrared data using an automated high-altitude lake validation site at lake tahoe. *IEEE Trans. Geosci. Remote Sens.* **2004**, *42*, 2767–2776. [[CrossRef](#)]
28. Jimenez-Munoz, J.C.; Cristóbal, J.; Sobrino, J.A.; Soria, G.; Ninyerola, M.; Pons, X. Revision of the single-channel algorithm for land surface temperature retrieval from landsat thermal-infrared data. *IEEE Trans. Geosci. Remote Sens.* **2009**, *47*, 339–349. [[CrossRef](#)]
29. Jimenez-Munoz, J.C.; Sobrino, J.A. A generalized single-channel method for retrieving land surface temperature from remote sensing data. *J. Geophys. Res. Atmos.* **2003**, *108*, 4688. [[CrossRef](#)]
30. Qin, Z.; Karnieli, A.; Berliner, P. A mono-window algorithm for retrieving land surface temperature from landsat tm data and its application to the Israel-Egypt border region. *Int. J. Remote Sens.* **2001**, *22*, 3719–3746. [[CrossRef](#)]
31. Ye, M.; Chen, H.M. Application and assessment of the one dimension vertical water temperature distribution model in geheyan reservoir. *Water Resour. Prot.* **2001**, *64*, 19–22. (In Chinese)
32. The United States Geological Survey Earth Explorer Website. Available online: <http://earthexplorer.usgs.gov> (accessed on 12 August 2017).
33. Bonnett, R.; Campbell, J.B. *Introduction to Remote Sensing*, 3rd ed.; Taylor & Francis: New York, NY, USA, 2002.
34. Lamaro, A.A.; Mariñelarena, A.; Torrusio, S.E.; Sala, S.E. Water surface temperature estimation from landsat 7 ETM+ thermal infrared data using the generalized single-channel method: Case study of Embalse del Río Tercero (Córdoba, Argentina). *Adv. Space Res.* **2013**, *51*, 492–500. [[CrossRef](#)]
35. Simon, R.; Tormos, T.; Danis, P.-A. Retrieving water surface temperature from archive landsat thermal infrared data: Application of the mono-channel atmospheric correction algorithm over two freshwater reservoirs. *Int. J. Appl. Earth Obs.* **2014**, *30*, 247–250. [[CrossRef](#)]
36. Atmospheric Correction Parameter Calculator. Available online: <http://atmcorr.gsfc.nasa.gov> (accessed on 20 November 2016).
37. Chander, G.; Markham, B. Revised landsat-5 tm radiometric calibration procedures and postcalibration dynamic ranges. *IEEE Trans. Geosci. Remote Sens.* **2003**, *41*, 2674–2677. [[CrossRef](#)]
38. Rodriguez-Galiano, V.; Pardo-Iguzquiza, E.; Sanchez-Castillo, M.; Chica-Olmo, M.; Chica-Rivas, M. Downscaling landsat 7 ETM+ thermal imagery using land surface temperature and NDVI images. *Int. J. Appl. Earth Obs.* **2012**, *18*, 515–527. [[CrossRef](#)]

